Implicit Large eddy simulation of hypersonic boundary-layer transition for a flared cone

Ngoc Cuong Nguyen*, Sebastien Terrana†, and Jaime Peraire‡
Department of Aeronautics and Astronautics, Massachusetts Institute of Technology, Cambridge, MA, 02139

We present an implicit large eddy simulation (ILES) of hypersonic boundary-layer transition for a flared cone at Mach number 6.0 and Reynolds number 10.8×10^6. The simulation is performed using a matrix-free discontinuous Galerkin (DG) method and a diagonally implicit Runge-Kutta (DIRK) scheme on graphics processor units (GPUs). A Jacobian-free Newton-Krylov (JFNK) method is used to solve nonlinear systems arising from the discretization of the Navier-Stokes equations. The ILES simulation exhibits the onset of primary and second-mode instabilities, quite zone, followed by transition to turbulence breakdown. These distinct characteristics of hypersonic flows on cone-like geometries are also observed in experiments. The Stanton number distribution and the pressure fluctuation are studied for different freestream intensities and compared with the experimental data. The results suggest that the ILES method is capable of capturing the onset of transition and turbulence breakdown phenomena for hypersonic turbulent flows past a flared cone.

I. Introduction

Many critical decisions in the design of hypersonic vehicles require the ability to predict accurately surface skin friction and aerodynamic heating which, in turn, depend on complex physical processes such as shock wave/boundary layer interaction, boundary layer separation, and laminar-to-turbulent transition. A deep understanding of the hypersonic boundary layers, including boundary layer transition, is crucial to the design of thermal protection systems and flight control for hypersonic vehicles. The prediction of hypersonic boundary layers presents a number of challenges. Despite considerable efforts in experimental, theoretical, and numerical studies, many critical physical mechanisms underlying the transition to turbulence in hypersonic boundary layers are not well understood [1, 2]. A unique feature of a hypersonic boundary layers is the presence of a family of acoustic instability modes, the Mack modes [3], in addition to the vorticity modes encountered in lower speed flows [4]. The Mack modes consist of high frequency, large amplitude density fluctuations and can dominate the transition process. The different instability modes combined with the nature of the free stream disturbances lead to many different paths to flow transition including natural transition, disturbance-induced transition, crossflow-induced transition, separation-induced transition, shock-induced transition, roughness-induced transition, nose bluntness entropy-layer on transition, bypass transition, and transition-reversal phenomena [5]. These unique multifaceted characteristics of hypersonic boundary layers make prediction a very difficult task. Gaining this understanding is often hampered by the difficulty to obtain high quality data to validate the theory and modeling efforts.

Numerical tools for turbulence studies still rely heavily on Reynolds–Averaged Navier—Stokes (RANS) models. RANS models are computationally affordable but are severely limited in their ability to model laminar-to-turbulent transition. In addition, RANS turbulence closure relations based on equilibrium assumptions have met limited success to model the rapidly distorting flow fields encountered in hypersonic shock boundary layer interactions and separated flows. Direct numerical simulation (DNS) resolves the whole range of spatial and temporal scales of the turbulence. In principle, DNS methods can accurately predict transition and the complex physical phenomena encountered in hypersonic shock layers. DNS is computationally expensive for predicting hypersonic turbulent flows of engineering interest. Large eddy simulation (LES) is an alternative approach which holds the promise to address the shortcomings of both RANS and DNS, and enable a step-change in the prediction of complex turbulent flows. With the advent of modern low-energy consumption highly scalable GPU architectures, both DNS and LES methods become affordable for

*Principal Research Scientist, Department of Aeronautics and Astronautics, Massachusetts Institute of Technology, Cambridge, MA, 02139. Email: cuongng@mit.edu. Senior AIAA member.

†Research Engineer, presently at CEA, DAM, DIF, F-91297 Arpajon, France. Email: sebastien.terrana@cea.fr.

‡Professor, Department of Aeronautics and Astronautics, Massachusetts Institute of Technology, Cambridge, MA, 02139. Email: peraire@mit.edu. AIAA Fellow.

a wide variety of turbulent flows. Nevertheless, RANS, LES and DNS are indispensable tools in turbulence research to provide the detailed physics that are not possible to be observed experimentally.

In the LES approach, the large-scale eddies of the flow field are resolved and the small scales are modeled using an appropriate model. When the small-scale eddies are directly resolved by using a fine computational grid and a small time-step size, the method is called direct numerical simulation (DNS). DNS remains prohibitive for turbulent flows at high Reynolds numbers due to the enormous amount of grid points required to resolve the small-scale eddies. When the number of grid points is not sufficient to resolve the small-scale eddies but enough to resolve the large-scale eddies, the method is called implicit LES (ILES) or sometimes referred to as under-resolved DNS (UDNS) [6]. In recent years, the use of discontinuous Galerkin (DG) methods for ILES of transitional and turbulent flows gains considerable attention from researchers in computational fluid dynamics [6–13]. It is shown in [14] that for moderate polynomial degrees (between 2 and 4), DG methods introduce numerical dissipation in under-resolved computations of convection-dominated flows, which acts as an implicit filter to dissipate the unresolved turbulent features. The numerical dissipation is localized near the Nyquist wavenumber and applied to the smallest resolved scales, while the amount of such dissipation depends mostly on the energy in those scales. Therefore, by choosing the element size h and the polynomial degree k, the numerical dissipation can be tuned to filter the unresolved scales appropriately.

Although low-order numerical schemes remain prominently use in computational fluid dynamics, high-order numerical schemes are increasingly used for LES and DNS computations of transitional and turbulent flows. Indeed, the prediction of transitional and turbulent flows relies on resolving wave propagation phenomena and small-scale flow features for which high-order accuracy is absolutely needed. High-order finite difference and finite element methods have been developed and increasingly used for simulating hypersonic flows. Recently, we have developed a matrix-free DG method for numerically solving computational fluid dynamics problems [15]. A key component in the method is the Jacobian-free Newton-Krylov (JFNK) solver that is based on the reduced basis approximation to construct a matrix-free preconditioner. The method is completely matrix-free in the sense that it does not need any part of the full Jacobian matrix. The matrix-free DG method has been implemented in the open-source code Exasim [16] and applied to hypersonic flows [17], and turbulent transonic flows [15].

The formation, propagation, and interaction of shock waves represent one of the challenging problems in hypersonic flows. Difficulties in simulating shock flows are that (1) at the very moment a shock is formed it poses a source of instability in the shock region, which then leads to numerical instabilities if no treatment of shock waves is introduced; (2) it is hard to predict when and where new shocks arise, and track them as they propagate through the physical domain and interact with each other and with boundary layers and vortices; and (3) numerical treatment of shock waves should not cause deterioration in resolution and reduction of accuracy in domains where the solution is smooth. In addition to shock waves, a number of other sharp features such as contact discontinuities, high thermal gradients, and thin shear layers may also appear in turbulent hypersonic flows. For high-order numerical methods, insufficient resolution or an inadequate treatment to capture these shocks often results in Gibbs oscillations, which can grow rapidly and contribute to numerical instabilities.

These above-mentioned challenges have been a driving force behind the development of shock capturing methods designed to detect and stabilize shocks. A number of shock detection methods rely on the non-smoothness of the numerical solution to detect shocks as well as other sharp features [18–28]. Among them, the sensor by Krivodonova *et al.* [24], devised in the context of DG methods, takes advantage of the theoretical convergence rate of DG schemes for smooth solutions in order to detect discontinuities. The shock sensor by Persson *et al.* [27, 28] is based on the decay rate of the coefficients of the DG polynomial approximation. Other methods that rely on high-order derivatives of the solution include [18–23, 25, 26], and apply to numerical schemes for which such derivatives can be computed, such as spectral-type methods and high-order finite difference methods. The most simple shock-detection method is to take advantage of the strong compression that a fluid undergoes across a shock wave and use the divergence of the velocity field as a shock sensor [29–31]. Shock stabilization methods lie within one of the following two categories: limiters and artificial viscosity. Limiters, in the form of flux limiters [32–34], slope limiters [24, 35–37], and WENO-type schemes [38–41] pose implementation difficulties for implicit time integration schemes and high-order methods on complex geometries. As for artificial viscosity methods, Laplacian-based [27, 28, 30, 31, 42–44] and physics-based [18–22, 25–27, 29, 45, 46] approaches have been proposed. An assessment of artificial viscosity methods for LES is presented in [47]. A more recent shock capturing scheme [48] aims to align mesh elements exactly along the shock waves and employ DG methods to handle shocks.

In this paper, we perform an implicit large eddy simulation (ILES) of hypersonic boundary-layer transition for a flared cone at Mach number 6.0 and Reynolds number 10.8×10^6. Hypersonic boundary-layer transition of a flared cone model (see Figure 1) has been experimentally investigated using BAM6QT at Purdue University [49, 50]. Recently,

DNS studies of the flared cone were reported in [50, 51]. It was found that the formation of the primary streaks is directly attributed to the steady streamwise vortices, which are generated by the fundamental resonance. The primary streaks disappear when these vortices are lifted up away from the wall. When these streamwise vortices break down and are pushed back toward the wall, the secondary streaks appear with an increased streak count in azimuthal direction. The similarities between the streak patterns observed in the experiments and the DNS results suggest that the transition is caused by a fundamental breakdown [51]. The ILES simulation exhibits the onset of primary and second-mode instabilities, quite zone, followed by transition to turbulence breakdown. These distinct characteristics of hypersonic flows on cone-like geometries are also observed in experiments. The Stanton number distribution and the pressure fluctuation are studied for different freestream intensities and compared with the experimental data. The results suggest that the ILES method is capable of capturing the onset of transition and turbulence breakdown phenomena for hypersonic turbulent flows past a flared cone. The present ILES simulation is performed using the matrix-free discontinuous Galerkin (DG) method with Jacobian-free Newton-Krylov (JFNK) solver [15]. The artificial viscosity method [29–31] is employed to capture shocks in our ILES computation.

II. Methodology

A. Governing equations

Let $t_f > 0$ be a final time and let $\Omega \subset \mathbb{R}^d$, $1 \leq d \leq 3$ be an open, connected and bounded physical domain with Lipschitz boundary $\partial\Omega$. The unsteady compressible Navier-Stokes equations in conservation form are given by

$$\boldsymbol{q} - \nabla \mathbf{u} = 0\,, \qquad \text{in } \Omega \times [0, t_f)\,, \tag{1a}$$

$$\frac{\partial \mathbf{u}}{\partial t} + \nabla \cdot \boldsymbol{F}(\mathbf{u}, \boldsymbol{q}) = 0\,, \qquad \text{in } \Omega \times [0, t_f)\,, \tag{1b}$$

$$\boldsymbol{B}(\mathbf{u}, \boldsymbol{q}) = 0\,, \qquad \text{on } \partial\Omega \times [0, t_f)\,, \tag{1c}$$

$$\mathbf{u} - \mathbf{u}_0 = 0\,, \qquad \text{on } \Omega \times \{0\}\,. \tag{1d}$$

Here, $\mathbf{u} = (\rho, \rho u_j, \rho E),\ j = 1, ..., d$ is the m-dimensional ($m = d + 2$) vector of conserved quantities, $\mathbf{u}_0$ is an initial state, $\boldsymbol{B}(\mathbf{u}, \boldsymbol{q})$ is a boundary operator, and $\boldsymbol{F}(\mathbf{u}, \boldsymbol{q})$ are the inviscid and viscous fluxes of dimensions $m \times d$,

$$\boldsymbol{F}(\mathbf{u}, \boldsymbol{q}) = \begin{pmatrix} \rho \boldsymbol{u} \\ \rho \boldsymbol{u} \otimes \boldsymbol{u} + p\boldsymbol{I} - \boldsymbol{\tau} \\ \boldsymbol{u}(\rho E + p) - \boldsymbol{\tau}\boldsymbol{u} + \boldsymbol{f} \end{pmatrix}, \tag{2}$$

where p denotes the thermodynamic pressure, $\boldsymbol{\tau}$ the viscous stress tensor, $\boldsymbol{f}$ the heat flux, and $\boldsymbol{I}$ is the identity tensor. For a calorically perfect gas in thermodynamic equilibrium, $p = (\gamma - 1)\left(\rho E - \rho\,|\boldsymbol{u}|^2/2\right)$, where $\gamma = c_p/c_v > 1$ is the ratio of specific heats and in particular $\gamma \approx 1.4$ for air. c_p and c_v are the specific heats at constant pressure and volume, respectively. For a Newtonian fluid with the Fourier's law of heat conduction, the viscous stress tensor and heat flux are given by

$$\tau_{ij} = \mu_f \left(\frac{\partial u_i}{\partial x_j} + \frac{\partial u_j}{\partial x_i} - \frac{2}{3}\frac{\partial u_k}{\partial x_k}\delta_{ij} \right) + \beta_f \frac{\partial u_k}{\partial x_k}\delta_{ij}, \qquad f_j = -\kappa_f \frac{\partial T}{\partial x_j}, \tag{3}$$

where T denotes temperature, μ_f the dynamic (shear) viscosity, β_f the bulk viscosity, $\kappa_f = c_p\,\mu_f/Pr$ the thermal conductivity, and Pr the Prandtl number; $Pr \approx 0.71$ for air, and $\beta_f = 0$ under the Stokes' hypothesis.

In order to deal with shock waves and discontinuities, we add artificial viscosities to the physical ones as follows:

$$\beta = \beta_f + \bar{\beta}^*, \qquad \mu = \mu_f + \bar{\mu}^*, \qquad \kappa = \kappa_f + \bar{\kappa}^*, \tag{4}$$

where $\bar{\beta}^*$, $\bar{\mu}^*$, and $\bar{\kappa}^*$ are the artificial bulk viscosity, artificial shear viscosity, and artificial thermal conductivity, respectively. The governing equations numerically discretized herein are still (1)-(3), where the physical viscosities of the fluid are replaced with those in (4). The artificial viscosities are defined in the next section.

B. Artificial viscosities

In this work, we modify the physics-based artificial viscosity approach introduced in our previous work [29, 30]. Specifically, we follow Fernandez et al. [29] without the artificial thermal conductivity which is designed for the strong

shocks appearing in hypersonic flows. This approach relies on a shock sensor. The *shock sensor*, evaluated pointwise, is constructed such that

$$s\left(\boldsymbol{x}\right) = s_d \cdot s_\omega, \qquad s_d = -\frac{h}{k}\frac{\nabla\cdot\boldsymbol{u}}{a^*}, \qquad s_\omega = \frac{\left(\nabla\cdot\boldsymbol{u}\right)^2}{\left(\nabla\cdot\boldsymbol{u}\right)^2 + |\nabla\times\boldsymbol{u}|^2 + \varepsilon}, \tag{5}$$

where ε is a constant of the order of the machine precision squared, k is the polynomial degree and a^* is the critical speed of sound. In Eq. (5) the dilatation sensor s_d is multiplied with Ducros's indicator [52] s_ω to avoid adding artificial viscosity to vortices. We define artificial viscosities as follows

$$\beta^* = \hat{s}\frac{k_\beta h}{k}\sqrt{|\boldsymbol{u}|^2 + a^{*2}}, \qquad \mu^* = k_\mu \beta^*\left(\boldsymbol{x}\right), \qquad \kappa^* = k_\kappa c_p\, \mu^*/Pr. \tag{6}$$

Here $k_{\beta,\mu,\kappa}$ are parameters that control the amount of artificial viscosities, and $\hat{s}$ denotes the smoothly bounded values of the shock sensor equations (5) and is given by

$$\hat{s}(\boldsymbol{x}) = \ell\big(s;\ s_0, s_{\max}\big), \tag{7}$$

The function ℓ represents a smooth approximation to the following limiting function $L(s; s_0, s_{\max}) = \min\{\max\{s - s_0, 0\} - s_{\max}, 0\} + s_{\max}$. In particular, it is defined as follows

$$\ell(s; s_0, s_{\max}) = \ell_{\min}(\ell_{\max}(s - s_0) - s_{\max}) + s_{\max}, \tag{8}$$

where

$$\begin{aligned} \ell_{\max}(s) &= \frac{s}{\pi}\arctan(100s) + \frac{s}{2} - \frac{1}{\pi}\arctan(100) + \frac{1}{2}, \\ \ell_{\min}(s) &= s - \ell_{\max}(s), \end{aligned} \tag{9}$$

Here the first parameter s_0 represents the starting point of the limiting function ℓ where it begins to increase with s, while the second parameter $s_{\max} > 0$ is the upper bound of the non-negative variable s. The parameters are chosen as $s_{\max} = 2$ and $s_0 = 0.01$ according to Fernandez et al. [29].

Since the original artificial viscosity fields (β^*, μ^*) are discontinuous, a node-averaging operator is applied to (β^*, μ^*) to make them C^0 continuous. The smooth reconstruction of the artificial viscosity field $\beta^*(\boldsymbol{x})$ is done by averaging all the multiple values of $\beta^*(\boldsymbol{x})$ along the element boundaries to obtain a continuous field $\bar{\beta}^*(\boldsymbol{x})$. The proposed reconstruction is particular to the DG discretization. Let $\boldsymbol{x}_n, 1 \le n \le n_k n_e$, be DG nodes of a high-order finite element mesh $\mathcal{T}_h$, where n_k is the number of nodes per element and n_e is the number of elements. For every node $\boldsymbol{x}_n$, $\bar{\beta}^*(\boldsymbol{x}_n) = \frac{1}{J_n}\sum_{j=1}^{J_n}\beta^*(\boldsymbol{x}_n)|_{K_j}$, where $K_j, 1 \le j \le J_n$, are all the elements in which $\boldsymbol{x}_n$ is located. If a mesh node $\boldsymbol{x}_n$ is located inside an element then $J_n = 1$, and it is located on a face then $J_n = 2$. If it is located on an edge or at an element vertex, then J_n is equal to the number of elements connected to that edge or that vertex, respectively. In essence, $\bar{\beta}^*(\boldsymbol{x}_n)$ is a polynomial of degree k on every element and continuous across element interfaces. Therefore, the present reconstruction is different from the elementwise linear reconstruction used in [29, 30].

C. Discontinuous Galerkin method

Let $\Omega \subseteq \mathbb{R}^d$ with $d = 3$ be a physical domain with Lipschitz boundary $\partial\Omega$. We denote by $\mathcal{T}_h$ a collection of disjoint, regular, k-th degree curved elements K that partition Ω, and set $\partial\mathcal{T}_h := \{\partial K : K \in \mathcal{T}_h\}$ to be the collection of the boundaries of the elements in $\mathcal{T}_h$. Let $\mathcal{P}^k(D)$ denote the space of complete polynomials of degree k on a domain $D \in \mathbb{R}^n$, let $L^2(D)$ be the space of square-integrable functions on D, and let $\boldsymbol{\psi}_K^k$ denote the k-th degree parametric mapping from the reference element K_{ref} to some element $K \in \mathcal{T}_h$ in the physical domain. We then introduce the following discontinuous finite element spaces:

$$\boldsymbol{Q}_h^k = \left\{\boldsymbol{r} \in [L^2(\mathcal{T}_h)]^{m\times d} \ :\ (\boldsymbol{r}\circ\boldsymbol{\psi}^k)|_K \in [\mathcal{P}^k(K_{ref})]^{m\times d}\ \ \forall K \in \mathcal{T}_h\right\},$$

$$\boldsymbol{\mathcal{V}}_h^k = \left\{\boldsymbol{w} \in [L^2(\mathcal{T}_h)]^{m} \ :\ (\boldsymbol{w}\circ\boldsymbol{\psi}^k)|_K \in [\mathcal{P}^k(K_{ref})]^{m}\ \ \forall K \in \mathcal{T}_h\right\},$$

where m denotes the number of equations of the conservation law, i.e. $m = d + 2$ for the Navier-Stokes system. Next, we define several inner products associated with these finite element spaces as

$$(\boldsymbol{w}, \boldsymbol{v})_{\mathcal{T}_h} = \sum_{K \in \mathcal{T}_h} (\boldsymbol{w}, \boldsymbol{v})_K = \sum_{K \in \mathcal{T}_h} \int_K \boldsymbol{w} \cdot \boldsymbol{v}, \tag{10a}$$

$$(\boldsymbol{W}, \boldsymbol{V})_{\mathcal{T}_h} = \sum_{K \in \mathcal{T}_h} (\boldsymbol{W}, \boldsymbol{V})_K = \sum_{K \in \mathcal{T}_h} \int_K \boldsymbol{W} : \boldsymbol{V}, \tag{10b}$$

$$\langle \boldsymbol{w}, \boldsymbol{v} \rangle_{\partial \mathcal{T}_h} = \sum_{K \in \mathcal{T}_h} \langle \boldsymbol{w}, \boldsymbol{v} \rangle_{\partial K} = \sum_{K \in \mathcal{T}_h} \int_{\partial K} \boldsymbol{w} \cdot \boldsymbol{v}, \tag{10c}$$

for $\boldsymbol{w}, \boldsymbol{v} \in \boldsymbol{\mathcal{V}}_h^k$, $\boldsymbol{W}, \boldsymbol{V} \in \boldsymbol{\mathcal{Q}}_h^k$, where $\cdot$ and $:$ denotes the scalar product and Frobenius inner product, respectively.

The DG discretization of the governing equations reads as follows: Find $\big(\boldsymbol{q}_h(t), \mathbf{u}_h(t)\big) \in \boldsymbol{\mathcal{Q}}_h^k \times \boldsymbol{\mathcal{V}}_h^k$ such that

$$\big(\boldsymbol{q}_h, \boldsymbol{r}\big)_{\mathcal{T}_h} + \big(\mathbf{u}_h, \nabla \cdot \boldsymbol{r}\big)_{\mathcal{T}_h} - \big\langle \widehat{\mathbf{u}}_h, \boldsymbol{r} \cdot \boldsymbol{n} \big\rangle_{\partial \mathcal{T}_h} = 0\,, \tag{11a}$$

$$\Big(\frac{\partial\, \mathbf{u}_h}{\partial t}, \boldsymbol{w}\Big)_{\mathcal{T}_h} - \Big(\boldsymbol{F}(\mathbf{u}_h, \boldsymbol{q}_h), \nabla \boldsymbol{w}\Big)_{\mathcal{T}_h} + \Big\langle \widehat{\boldsymbol{f}_h}(\mathbf{u}_h, \boldsymbol{q}_h), \boldsymbol{w} \Big\rangle_{\partial \mathcal{T}_h} = 0\,, \tag{11b}$$

for all $(\boldsymbol{r}, \boldsymbol{w}) \in \boldsymbol{\mathcal{Q}}_h^k \times \boldsymbol{\mathcal{V}}_h^k$ and all $t \in [0, t_f)$, as well as

$$\big(\mathbf{u}_h|_{t=0} - \mathbf{u}_0, \boldsymbol{w}\big)_{\mathcal{T}_h} = 0\,, \tag{11c}$$

for all $\boldsymbol{w} \in \boldsymbol{\mathcal{V}}_h^k$. Here $\widehat{\mathbf{u}}_h$ is the numerical trace and $\widehat{\boldsymbol{f}_h}$ is the numerical flux. For DG methods, both the numerical trace and flux must be continuous across element boundaries. The general form of the numerical trace and flux on the interior faces that satisfies the continuity requirement is given by

$$\begin{aligned} \widehat{\mathbf{u}}_h &= \frac{1}{2}(\mathbf{u}_h^+ + \mathbf{u}_h^-) + (\mathbf{u}_h^+ \boldsymbol{\beta} \cdot \boldsymbol{n}^+ + \mathbf{u}_h^- \boldsymbol{\beta} \cdot \boldsymbol{n}^-) + \boldsymbol{\gamma} \cdot (\boldsymbol{q}_h^+ \cdot \boldsymbol{n}^+ + \boldsymbol{q}_h^- \cdot \boldsymbol{n}^-), \\ \widehat{\boldsymbol{f}_h} &= \frac{1}{2}\left(\boldsymbol{F}(\mathbf{u}_h^+, \boldsymbol{q}_h^+) + \boldsymbol{F}(\mathbf{u}_h^-, \boldsymbol{q}_h^-)\right) \cdot \boldsymbol{n}^+ + \boldsymbol{\sigma} \cdot (\mathbf{u}_h^+ - \mathbf{u}_h^-), \end{aligned} \tag{12}$$

where $\boldsymbol{\beta}$ is a vector-valued function, and $\boldsymbol{\gamma}, \boldsymbol{\sigma}$ are a matrix-valued function. Note that $\mathbf{u}_h^+ = \mathbf{u}_h|_{F \in K^+}$ and $\mathbf{u}_h^- = \mathbf{u}_h|_{F \in K^-}$ denote the restriction of the numerical solution $\mathbf{u}_h$ on interior face F shared by elements K^+ and K^-. On the boundary faces, the definition of the numerical trace and flux depends on the boundary conditions. For the computation performed herein, there are two types of boundary conditions, namely, far-field condition and adiabatic wall condition. We refer to [6, 53] for the implementation of these two boundary conditions.

Different choices of the stabilization functions $\boldsymbol{\beta}, \boldsymbol{\gamma}, \boldsymbol{\sigma}$ result in different DG methods. The LDG method [54] corresponds to $\boldsymbol{\gamma} = 0$, the second Bassi-Rebay (BR2) method [55] to $\boldsymbol{\beta} = \boldsymbol{\gamma} = 0$, and the first Bassi-Rebay (BR1) method [56] to $\boldsymbol{\beta} = \boldsymbol{\gamma} = \boldsymbol{\sigma} = 0$. These stabilization functions play an important role in the stability and accuracy of the resulting DG method. Indeed, it is known that the BR1 method is not stable for elliptic problems [57]. The hybridized DG (HDG) method [6, 53] does not define the numerical trace $\widehat{\boldsymbol{u}}_h$ terms of the approximate solution. In the HDG method, the numerical trace $\widehat{\mathbf{u}}_h$ becomes a dependent variable to be solved together with $(\mathbf{u}_h, \boldsymbol{q}_h)$ by introducing another equation that weakly imposes the continuity of the numerical flux. The HDG method is computationally efficient when we form and solve the matrix system because it results in smaller matrix system than the LDG method and the BR2 method. However, the HDG method is not suited to our matrix-free approach because computing the residual of the HDG method involves solving nonlinear local problems for $(\boldsymbol{q}_h, \mathbf{u}_h)$ in terms of $\widehat{\mathbf{u}}_h$. Hence, it would be computationally expensive to use the HDG method within the JFNK approach.

In this paper, the BR2 method is used to discretize the compressible Navier-Stokes equations in space since it is suited to the matrix-free solution method introduced in the next section. Herein we choose $\boldsymbol{\beta} = \boldsymbol{\gamma} = 0$ and $\boldsymbol{\sigma} = \lambda_{max}(\widehat{\mathbf{u}}_h)\, \boldsymbol{I}$, where λ_{max} denotes the maximum-magnitude eigenvalue of $\boldsymbol{A}_n(\mathbf{u}_h) = [\partial \boldsymbol{F}_{\text{inv}}(\mathbf{u}_h)/\partial \mathbf{u}] \cdot \boldsymbol{n}$ with $\boldsymbol{F}_{\text{inv}}$ being the inviscid part of the flux function $\boldsymbol{F}$. For general convection-diffusion problems, the stabilization term $\boldsymbol{\sigma}$ should include both the convection-stabilizing term $\boldsymbol{\sigma}_c$ and the diffusion-stabilizing term $\boldsymbol{\sigma}_d$, namely $\boldsymbol{\sigma} = \boldsymbol{\sigma}_c + \boldsymbol{\sigma}_d$, so that the resulting scheme can be stable in both pure convection limit and pure diffusion limit. The convection-stabilizing term is usually computed by using approximate Riemann solvers such as HLL/HLLC schemes, Roe's scheme, and Lax-Friedrich scheme, while

the diffusion-stabilizing term is proportional to the diffusion coefficient. Because our particular problem presented in the next section is strongly convection-dominated, the diffusion-stabilizing term $\sigma_d \sim 1/Re$ can be neglected. See [6, 53, 58, 59] for additional discussion on the stabilization of DG methods.

For computational efficiency, we can eliminate $\boldsymbol{q}_h$ to obtain a new system in terms of $\mathbf{u}_h$ only as follows. It follows from (11a) and (12) that

$$\boldsymbol{q}_h = \nabla \mathbf{u}_h + \mathcal{L}(\mathbf{u}_h) \tag{13}$$

where $\mathcal{L}(\mathbf{u}_h) \in \mathcal{P}^k(K)$ is solved in an element-by-element fashion as follows

$$\big(\mathcal{L}(\mathbf{u}_h), \boldsymbol{r}\big)_K = \big\langle \widehat{\mathbf{u}}_h - \mathbf{u}_h, \boldsymbol{r} \cdot \boldsymbol{n} \big\rangle_{\partial K}, \quad \forall \boldsymbol{r} \in \mathcal{P}^k(K), \tag{14}$$

for every element $K \in \mathcal{T}_h$. Since $\widehat{\mathbf{u}}_h$ depends linearly on $\mathbf{u}_h$, $\boldsymbol{q}_h$ also linearly depends on $\mathbf{u}_h$. Hence, we can substitute (13) into (11b) to obtain the following weak form: Find $\mathbf{u}_h(t) \in \boldsymbol{\mathcal{V}}_h^k$ such that

$$\Big(\frac{\partial \mathbf{u}_h}{\partial t}, \boldsymbol{w}\Big)_{\mathcal{T}_h} - \Big(\boldsymbol{F}(\mathbf{u}_h, \mathcal{D}(\mathbf{u}_h)), \nabla \boldsymbol{w}\Big)_{\mathcal{T}_h} + \Big\langle \widehat{\boldsymbol{f}}_h(\mathbf{u}_h, \mathcal{D}(\mathbf{u}_h)), \boldsymbol{w} \Big\rangle_{\partial \mathcal{T}_h} = 0, \tag{15}$$

for all $\boldsymbol{w} \in \boldsymbol{\mathcal{V}}_h^k$, where $\mathcal{D}(\mathbf{u}_h) = \nabla \mathbf{u}_h + \mathcal{L}(\mathbf{u}_h)$. The above weak formulation can be written as a system of ordinary differential equations in matrix form as follows:

$$\boldsymbol{M} \frac{d\mathbf{u}}{dt} + \boldsymbol{g}(\mathbf{u}) = 0, \tag{16}$$

where $\mathbf{u}$ is the vector of degrees of freedom of $\mathbf{u}_h$, $\boldsymbol{M}$ is the mass matrix, and $\boldsymbol{g}(\mathbf{u})$ is a nonlinear vector-valued function corresponding to the last two terms of (15).

Finally, the semi-discrete system (16) is further discretized in time using L-stable diagonally implicit Runge-Kutta (DIRK) schemes [60]. The use of L-stable DIRK methods for the temporal discretization is important to maintain accuracy and stability because the DG discretization of turbulent shock flows at high Reynolds number results in very stiff nonlinear ODE systems. If the use of an implicit time scheme allows to alleviate the CFL limitation on the timestep size, the latter cannot be arbitrary large in practice. Whenever LES or DNS are the aim, the timestep has to be small enough to resolve the viscous time scales

D. Jacobian-free Newton-Krylov solver

The main goal of the JFNK approach [61] is to avoid forming the Jacobian matrix and construct an effective preconditioner to reduce the number of GMRES iterations. As discussed in great detail in [61], there are a wide variety of preconditioning techniques from incomplete LU (ILU) factorizations, multigrid methods, Schwarz-based domain decomposition methods, physics-based preconditioning, and matrix-free preconditioning methods. A number of preconditioning techniques such as ILU still form matrices that are reduced in complexity as compared to the full Jacobian. Storage and memory bandwidth limitations provide a motive for preconditioning approaches that do not require the formation of any matrix. We employ the JFNK method to solve nonlinear and linear systems arising from the numerical discretization of the Navier-Stokes equations.

Newton's method is used to solve the nonlinear system of equations, $\boldsymbol{R}(\mathbf{u}^n) = 0$, resulting from the temporal discretization of the system (16), where $\mathbf{u}^n \in \mathbb{R}^{n_{\text{dof}}}$ is the vector of degrees of freedom of $\mathbf{u}_h^n$ and $\boldsymbol{R}(\cdot) \in \mathbb{R}^{n_{\text{dof}}}$ is the residual vector. We note that $n_{\text{dof}} = (d+2)n_k n_e$, where n_k is the number of DG nodes per element and n_e is the number of elements. Furthermore, the time-stage step is given by $n = (n_t - 1)n_s + s$, where n_t is the n_t^{th} timestep, n_s is the number of stages for a DIRK scheme, and s is the s^{th} stage. For every m^{th} iteration of the Newton method, we use GMRES to solve the resulting linear system

$$\boldsymbol{J}(\mathbf{u}^{n,m}) \delta \mathbf{u}^{n,m} = -\boldsymbol{R}(\mathbf{u}^{n,m}), \tag{17}$$

for the Newton increment $\delta \mathbf{u}^{n,m}$, where $\boldsymbol{J}(\mathbf{u}^{n,m}) = \partial \boldsymbol{R}(\mathbf{u}^{n,m})/\partial \mathbf{u}$ is the Jacobian matrix. In what follows, we shall drop the superscript m to simplify the notation. Hence, the superscript n should be understood as the superscript n, m in the remainder of this section.

We construct a reduced basis (RB) approximation [62–64] to $\delta \mathbf{u}^n$ and use it as an initial guess in order to accelerate the GMRES method. Given a reduced basis $\boldsymbol{W}_n = \text{span}\{\delta \mathbf{u}^{n-j}, 1 \le j \le n_{\text{rb}}\}$ consisting of n_{rb} previous solution vectors

of the linear systems, the RB approximation to $\delta\mathbf{u}^n$ is computed as the best least squares solution of the following problem

$$\delta\mathbf{u}^n_{\text{rb}} = \arg\min_{\delta\mathbf{w}\in\boldsymbol{W}_n} \|\boldsymbol{J}(\mathbf{u}^n)\delta\mathbf{w} + \boldsymbol{R}(\mathbf{u}^n)\|\,. \tag{18}$$

It thus follows that $\delta\mathbf{u}^n_{\text{rb}} = \boldsymbol{W}_n\boldsymbol{a}^n_{\text{rb}}$, where $\boldsymbol{a}^n_{\text{rb}} \in \mathbb{R}^{n_{\text{rb}}}$ is the solution of the RB system, $\boldsymbol{J}_{\text{rb}}(\mathbf{u}^n)\boldsymbol{a}^n_{\text{rb}} = -\boldsymbol{R}_{\text{rb}}(\mathbf{u}^n)$, with $\boldsymbol{J}_{\text{rb}}(\mathbf{u}^n) = (\boldsymbol{J}(\mathbf{u}^n)\boldsymbol{W}_n)^T(\boldsymbol{J}(\mathbf{u}^n)\boldsymbol{W}_n)$ and $\boldsymbol{R}_{\text{rb}}(\mathbf{u}^n) = (\boldsymbol{J}(\mathbf{u}^n)\boldsymbol{W}_n)^T\boldsymbol{R}(\mathbf{u}^n)$. Forming the RB system requires $\boldsymbol{J}(\mathbf{u}^n)\boldsymbol{W}_n$ which is approximately computed by the finite difference (20). Typically, we set $n_{\text{rb}} = 5$, the cost of inverting the RB system is thus negligible. The RB approximation $\delta\mathbf{u}^n_{\text{rb}}$ is used as the initial guess in the GMRES method that solves (17) for $\delta\mathbf{u}^n$. We thus obtain $\delta\mathbf{u}^n = \delta\mathbf{v}^n + \delta\mathbf{u}^n_{\text{rb}}$, where $\delta\mathbf{v}^n$ is the best least squares solution of the following problem

$$\delta\mathbf{v}^n = \arg\min_{\delta\mathbf{w}\in\mathcal{K}_r(\boldsymbol{J}(\mathbf{u}^n),\boldsymbol{b}(\mathbf{u}^n))} \|\boldsymbol{J}(\mathbf{u}^n)\delta\mathbf{w} + \boldsymbol{b}(\mathbf{u}^n)\|\,, \quad \text{with } \boldsymbol{b}(\mathbf{u}^n) = \boldsymbol{R}(\mathbf{u}^n) + \boldsymbol{J}(\mathbf{u}^n)\delta\mathbf{u}^n_{\text{rb}}. \tag{19}$$

Here $\mathcal{K}_r(\boldsymbol{J}(\mathbf{u}^n), \boldsymbol{b}(\mathbf{u}^n)) = \text{span}\{\boldsymbol{b}(\mathbf{u}^n), \boldsymbol{J}(\mathbf{u}^n)\boldsymbol{b}(\mathbf{u}^n), \ldots, (\boldsymbol{J}(\mathbf{u}^n)^r\boldsymbol{b}(\mathbf{u}^n)\}$ is the Krylov subspace at the rth iteration. Therefore, it follows from (18) and (19) that our method is similar to the restarted GMRES method. The main difference between our method and the restarted GMRES method is that the restarted GMRES method uses the Krylov subspace $\mathcal{K}_r(\boldsymbol{J}(\mathbf{u}^n), \boldsymbol{R}(\mathbf{u}^n))$, whereas our method uses the RB space $\boldsymbol{W}_n$ for the first outer iteration. Furthermore, we make use of the reduced basis $\boldsymbol{W}_n$ to construct a matrix-free preconditioner to be used in the GMRES method for solving (19). The idea lies in the construction of an approximation to the Jacobian matrix $\boldsymbol{J}(\mathbf{u}^n)$ through a suitable low-rank approximation. We refer to [15] for a detailed discussion of the preconditioner.

Our solution method requires the computation of $\boldsymbol{J}(\mathbf{u}^n)\boldsymbol{W}_n$ which can be expensive if we have to form the Jacobian matrix $\boldsymbol{J}(\mathbf{u}_n)$ and perform matrix-matrix multiplication. Instead, the product of the Jacobian matrix with any vector $\boldsymbol{y}$ can be approximately computed by the Taylor expansion as follows

$$\boldsymbol{J}(\mathbf{u}^n)\,\boldsymbol{y} \approx \frac{\boldsymbol{R}(\mathbf{u}^n + \epsilon\boldsymbol{y}) - \boldsymbol{R}(\boldsymbol{u}^n)}{\epsilon}\,, \tag{20}$$

for small enough ϵ. We see that computing $\boldsymbol{J}(\mathbf{u}^n)\boldsymbol{W}_n = [\boldsymbol{J}(\mathbf{u}^n)\delta\mathbf{u}^{n-1}\ \boldsymbol{J}(\mathbf{u}^n)\delta\mathbf{u}^{n-2}\ \ldots\ \boldsymbol{J}(\mathbf{u}^n)\delta\mathbf{u}^{n-n_{\text{rb}}}]$ requires n_{rb} residual evaluations. In actual practice, we replace $\boldsymbol{J}(\mathbf{u}^n)\boldsymbol{W}_n$ with $\boldsymbol{U}_n = [\boldsymbol{J}(\mathbf{u}^n)\delta\mathbf{u}^{n-1}\ \boldsymbol{J}(\mathbf{u}^{n-1})\delta\mathbf{u}^{n-2}\ \ldots\ \boldsymbol{J}(\mathbf{u}^{n+1-n_{\text{rb}}})\delta\mathbf{u}^{n-n_{\text{rb}}}]$. Because only the first column of $\boldsymbol{U}_n$ has to be computed, while the remaining columns were already computed and stored, only one residual evaluation is required to form $\boldsymbol{U}_n$. By using $\boldsymbol{U}_n$ in place of $\boldsymbol{J}(\mathbf{u}^n)\boldsymbol{W}_n$ to compute the GMRES initial guess and construct the preconditioner, we reduce the number of residual evaluations from n_{rb} to 1. Henceforth, both the GMRES initial guess and the preconditioner add little to the overall cost since its computational cost can be far smaller than the residual evaluations required during the GMRES iterations.

E. Synthetic turbulence generation

Physically realistic boundary conditions are essential to obtaining accurate turbulence simulations. One of the most important boundary conditions is turbulent inflow condition at the inlet, where a time-varying flow field has to be specified for the resolved length scales. These inflow fluctuations must emulate the real turbulence for the problem being studied because they affect the downstream flow dynamics and, in turn, the realism of the entire simulation. Therefore, it is crucial to construct a time-varying flow field at the inflow boundary that can emulate the upstream turbulence disturbance. In order to study the effects of free-stream disturbances on boundary-layer transition of hypersonic flows, we employ the synthetic random Fourier method proposed by Kraichnan [65] and further developed by Bechara et al. [66], and Bailly and Juvé [67] to generate a synthetic turbulence field at the inflow boundary.

The velocity field at the inflow boundary is given by

$$\boldsymbol{v}_{\text{in}}(\boldsymbol{x}, t) = \bar{\boldsymbol{v}}(\boldsymbol{x}) + \boldsymbol{v}'(\boldsymbol{x}, t) \tag{21}$$

where $\bar{\boldsymbol{v}}$ is the mean flow and $\boldsymbol{v}'$ is a synthetic fluctuation field

$$\boldsymbol{v}'(\boldsymbol{x}, t) = 2\sum_{n=1}^{N} \hat{u}_n(t)\boldsymbol{\sigma}_n \cos(\boldsymbol{k}_n \cdot (\boldsymbol{x} - \boldsymbol{v}_c t) + \psi_n + \omega_n t). \tag{22}$$

Here $\hat{u}_n$, ψ_n, $\boldsymbol{\sigma}_n$, ω_n are amplitude, phase, direction, and angular frequency of the nth Fourier mode, respectively. The wave vector $\boldsymbol{k}_n$ is chosen randomly on a sphere with radius k_n to ensure isotropy of the generated velocity field. The

convective velocity $\boldsymbol{v}_c$ can be taken the same as the mean flow $\bar{\boldsymbol{v}}$. The energy spectrum for isotropic turbulence is simulated by a von Kármán-Pao spectrum

$$E(k) = \alpha \frac{I^2 u_\infty^2}{k_e} \frac{(k/k_e)^4}{[1 + (k/k_e)^2]^{17/6}} e^{-2(k/k_\eta)^2}, \tag{23}$$

where I is the freestream intensity, u_∞ is the freestream velocity, k is the wave number, $k_e = 9\pi\alpha(55\Lambda)^{-1}$ is the wave number at the peak of the energy spectrum, $k_\eta = \varepsilon^{1/4}\nu^{-3/4}$ is the Kolmogorov wave number, ν is the molecular viscosity, $\varepsilon = \beta(u_\infty I)^3\Lambda^{-1}$ is the dissipation rate, and Λ is the turbulence length scale. The two constants are determined as $\alpha = 1.453$ and $\beta = 0.3019$.

The turbulence length scale is set to $\Lambda = 10h_{\min}$, where $h_{\min}$ is the minimum grid length at the wall. We perform LES computations for several different values of freestream intensity I to study the effects of freestream disturbances on the boundary-layer transition. The numerical results are presented in the next section.

III. Results and Discussions

A. Problem description

HBL transition of a flared cone model (see Figure 1) has been experimentally investigated using BAM6QT at Purdue University [49, 50]. Recently, DNS studies of the flared cone were reported in [50, 51]. It was found that the formation of the primary streaks is directly attributed to the steady streamwise vortices, which are generated by the fundamental resonance. The primary streaks disappear when these vortices are lifted up away from the wall. When these streamwise vortices break down and are pushed back toward the wall, the secondary streaks appear with an increased streak count in azimuthal direction. The similarities between the streak patterns observed in the experiments and the DNS results suggest that the transition is caused by a fundamental breakdown. However, the peak Stanton number for the DNS is significantly larger as compared to the peak value observed in experiments. These differences arise due to the modeling assumptions of the controlled breakdown as compared to the natural transition observed at the BAM6QT.

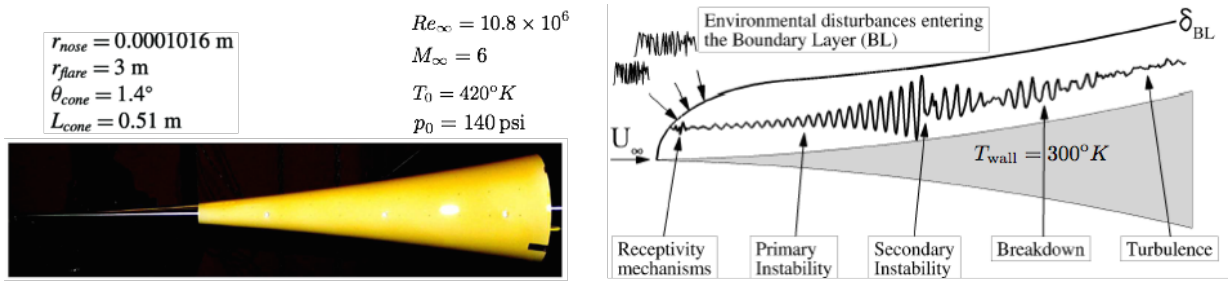

Fig. 1 Geometry parameters and flow conditions of the Purdue flared cone [51].

B. Flow statistics and comparisons to experiment

To study the effects of freestream disturbance on the HBL transition of the Purdue flared cone and thus better represent the expemental condition, we carry out DNS studies of the Purdue flared cone for three different turbulence intensities $I = 0.125\%, 0.25\%$, and 0.5% by using our in-house code `Exasim` [16]. The computational grid has more than 6 millions of quadratic hexahedral elements. The DIRK(3,3) scheme is used for temporal discretization with step size 0.00005 and 35,000 time steps. All of the DNS simulations were performed using 48 nodes (288 V100 GPUs) of the Summit Supercomputer and took 15 hours of run time. Figure 3 shows the side view of the computed instantaneous pressure and temperature in comparison with Schlieren images obtained by Zhang et. al. [68]. Several similar flow features are observed in both DNS results and experiments. Figure 4 depicts the top view of the computed instantaneous pressure and reveals the onset of transition and turbulence. Free-stream disturbance excites the second-mode instability. This instability is two-dimensional and similar to an acoustic wave trapped between a surface and the sonic line within the boundary layer. As the second-mode instability packet grows downstream, formation and growth of Görtler vortices occurs. Due to the second-mode instability and the formation of the Görtler vortices, the pressure fluctuations increase rapidly and reach a sufficient magnitude to cause the vortices to breakdown. Transition to turbulence begins and the flow becomes fully turbulent.

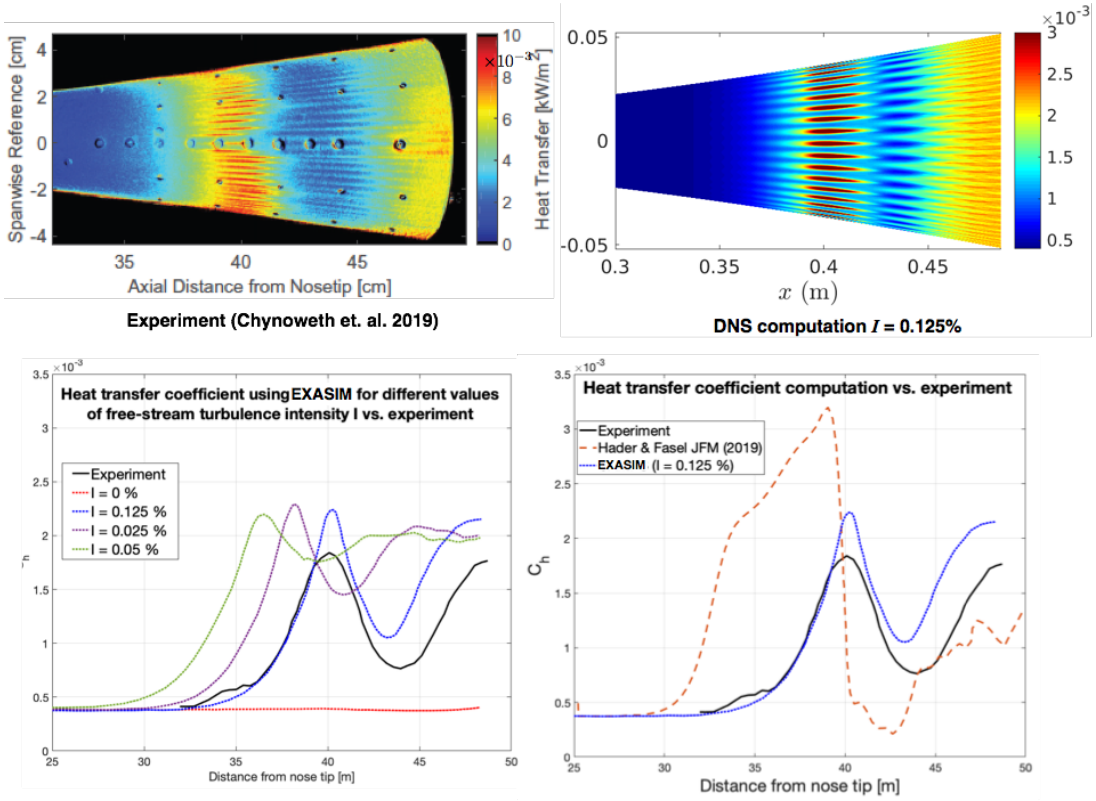

Fig. 2 Comparison of heat transfer coefficient between our DNS results, the experimental data obtained by Chynoweth et. al [50], and the DNS data obtained by Hader and Fasel [51].

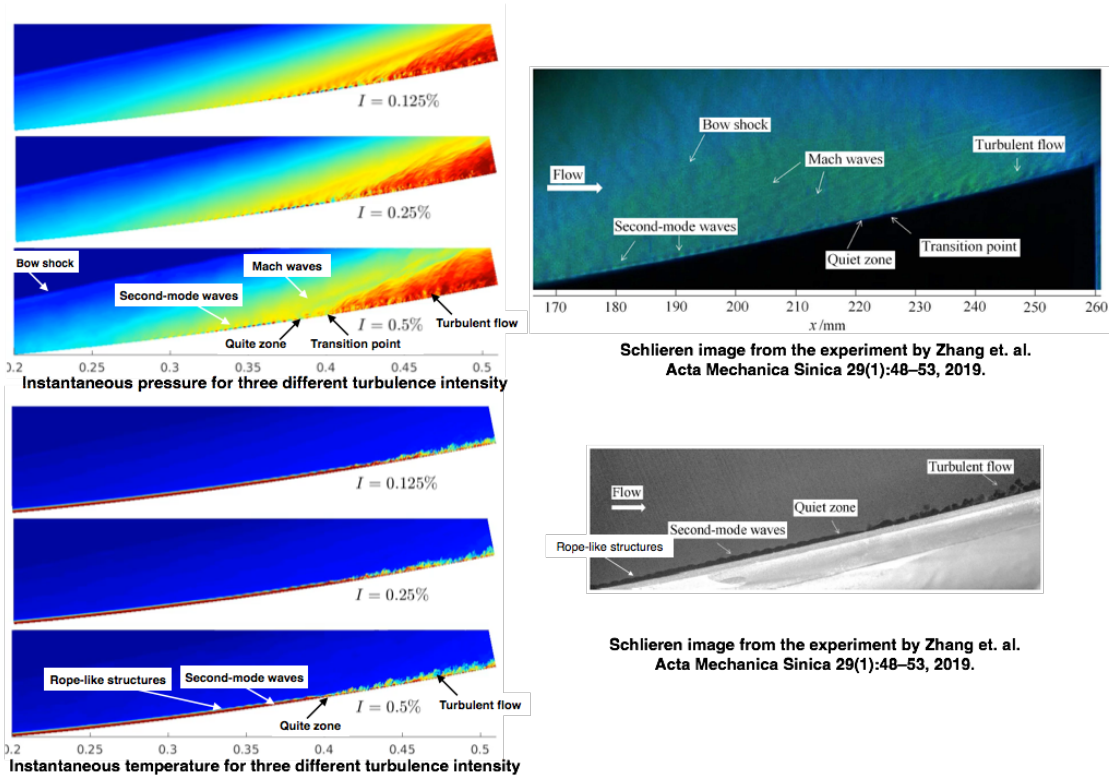

Fig. 3 Comparison of flow characteristics between the DNS results (left) and the experiments (right).

Comparisons with the experimental data as well as the DNS simulation [50] for the heat transfer coefficient are shown in Figure 2. We observe that the heat transfer coefficient obtained with our DNS for $I = 0.125\%$ agrees very well with the experimental data for $x < 0.4$ m. For $x > 0.4$ m, our DNS prediction is a little higher than the experimental data. Interestingly, the heat transfer rises rapidly during the growth of the second-mode instability and reaches its peak when the Görtler vortices begin to form. Then it decreases rapidly when the Görtler vortices grow as these vortices carry heat away from the cone surface, and reaches its trough when the Görtler vortices break up and transition occurs at this location. The heat transfer rises rapidly again when the flow becomes fully developed turbulent. Our DNS results show that HBL transition is sensitive to freestream disturbances resulting in the development and growth of the second-mode waves and the subsequent breakdown of the Görtler vortices. The good agreement between the computed heat transfer and the experimental data before the peak of the heat transfer coefficient suggests that the natural transition observed in the experiments is initiated by the receptivity of HBLs to freestream disturbances.

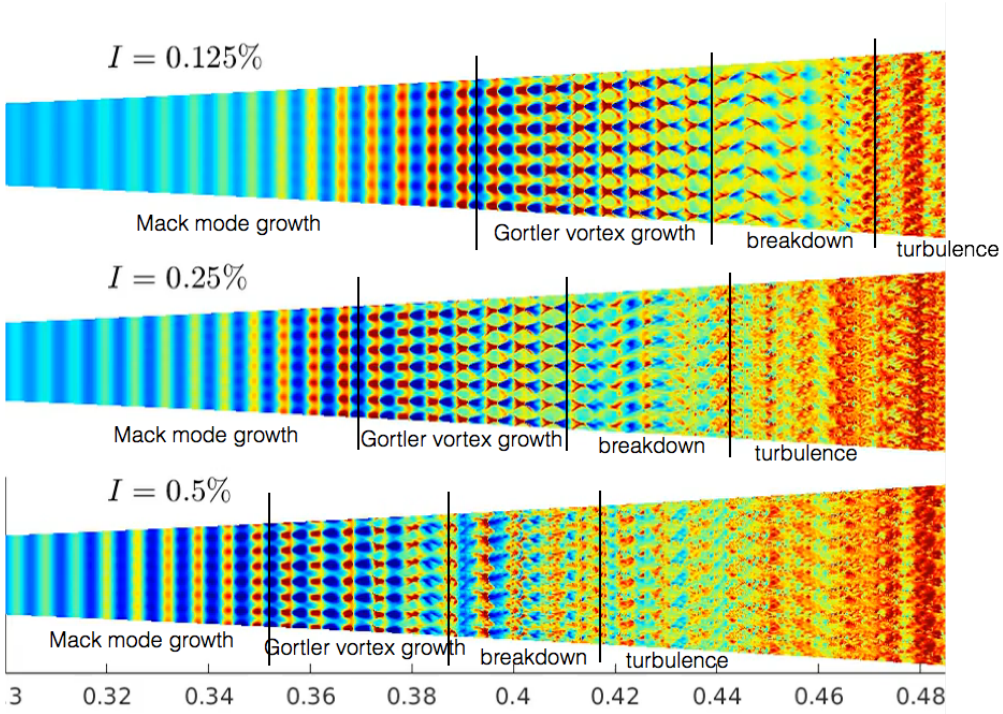

Fig. 4 Instantaneous pressure distributions on the flared cone surface show the growth of second-mode waves and Gorler's vortices, as well as their breakdown to turbulence.

IV. Conclusions

We performed an implicit large eddy simulation of hypersonic boundary-layer transition for a flared cone using a matrix-free DG method on graphics processor units. The ILES simulation exhibits the onset of primary and second-mode instabilities, quite zone, followed by transition to turbulence breakdown. These distinct characteristics of hypersonic flows on cone-like geometries are also observed in experiments. The Stanton number distribution and the pressure fluctuation are studied for different freestream intensities and compared with the experimental data. The ILES method was able to capture the onset of transition and turbulence breakdown phenomena for hypersonic turbulent flows past the flared cone. The heat transfer coefficient of the ILES computation agrees well with the experimental value up to the point of the onset of turbulence and is slightly larger than the experimental value after the breakdown to turbulence. The ILES computation did not consider real gas effects since nonequilibrium gas effects are not significant for the free-stream Mach number 6. Many hypersonic flows of interest involve higher Mach numbers and, in such cases, high-temperature nonequilibrium effects need to be considered. Therefore, future work will have to take real gas effects into account for modeling thermal and chemical non-equilibrium hypersonic flows.

Acknowledgments

We gratefully acknowledge the United States Department of Energy under contract DE-NA0003965 for supporting this work. The authors would like to thank the Oak Ridge Leadwership Computing Facility for providing access to their GPU clusters.

References

[1] Schneider, S. P., "Developing mechanism-based methods for estimating hypersonic boundary-layer transition in flight: The role of quiet tunnels," *Progress in Aerospace Sciences*, Vol. 72, 2015, pp. 17–29. doi:10.1016/J.PAEROSCI.2014.09.008, URL https://www.sciencedirect.com/science/article/pii/S0376042114000876.

[2] Zhong, X., and Wang, X., "Direct numerical simulation on the receptivity, instability, and transition of hypersonic boundary layers," *Annual Review of Fluid Mechanics*, Vol. 44, No. 1, 2012, pp. 527–561. doi:10.1146/annurev-fluid-120710-101208, URL http://www.annualreviews.org/doi/10.1146/annurev-fluid-120710-101208.

[3] Mack, L. M., "Boundary-layer linear stability theory," *AGARD Spec. Course on Stability and Transition of Laminar Flow*, 1984. URL https://apps.dtic.mil/docs/citations/ADP004046.

[4] Stetson, K., and Kimmel, R., "On hypersonic boundary-layer stability," *30th Aerospace Sciences Meeting and Exhibit*, Reston, Virigina, 1992, pp. AIAA–737. doi:10.2514/6.1992-737, URL http://arc.aiaa.org/doi/10.2514/6.1992-737.

[5] Fedorov, A., "Transition and stability of high-speed boundary layers," *Annual Review of Fluid Mechanics*, Vol. 43, No. 1, 2011, pp. 79–95. doi:10.1146/annurev-fluid-122109-160750, URL http://www.annualreviews.org/doi/10.1146/annurev-fluid-122109-160750.

[6] Fernandez, P., Nguyen, N. C., and Peraire, J., "The hybridized discontinuous Galerkin method for implicit large-eddy simulation of transitional turbulent flows," *Journal of Computational Physics*, Vol. 336, 2017, pp. 308–329. doi:10.1016/j.jcp.2017.02.015.

[7] Beck, A. D., Bolemann, T., Flad, D., Frank, H., Gassner, G. J., Hindenlang, F., and Munz, C.-D., "High-order discontinuous Galerkin spectral element methods for transitional and turbulent flow simulations," *International Journal for Numerical Methods in Fluids*, Vol. 76, No. 8, 2014, pp. 522–548. doi:10.1002/fld.3943, URL http://doi.wiley.com/10.1002/fld.3943.

[8] Frere, A., Hillewaert, K., Chivaee, H. S., Mikkelsen, R. F., and Chatelain, P., "Cross-validation of mumerical and experimental studies of transitional airfoil performance," *33rd Wind Energy Symposium*, AIAA SciTech Forum, American Institute of Aeronautics and Astronautics, 2015. doi:doi:10.2514/6.2015-0499, URL https://doi.org/10.2514/6.2015-0499.

[9] Gassner, G. J., and Beck, A. D., "On the accuracy of high-order discretizations for underresolved turbulence simulations," *Theoretical and Computational Fluid Dynamics*, Vol. 27, 2013, pp. 221–237. doi:10.1007/s00162-011-0253-7.

[10] Murman, S. M., Diosady, L., Garai, A., and Ceze, M., "A space-time discontinuous-Galerkin approach for separated flows," *54th AIAA Aerospace Sciences Meeting*, 2016, pp. AIAA–2016–1059. doi:doi:10.2514/6.2016-1059, URL https://doi.org/10.2514/6.2016-1059.

[11] Renac, F., de la Llave Plata, M., Martin, E., Chapelier, J. B., and Couaillier, V., "Aghora: A high-order DG solver for turbulent flow simulations," Springer International Publishing, Cham, 2015, pp. 315–335. doi:10.1007/978-3-319-12886-3_15, URL https://doi.org/10.1007/978-3-319-12886-3{_}15.

[12] Uranga, A., Persson, P.-O., Drela, M., and Peraire, J., "Implicit large eddy simulation of transition to turbulence at low Reynolds numbers using a discontinuous Galerkin method," *International Journal for Numerical Methods in Engineering*, Vol. 87, No. 1-5, 2011, pp. 232–261. doi:10.1002/nme.3036, URL http://dx.doi.org/10.1002/nme.3036.

[13] de Wiart, C. C., and Hillewaert, K., "Development and validation of a massively parallel high-order solver for DNS and LES of industrial flows," Springer International Publishing, Cham, 2015, pp. 251–292. doi:10.1007/978-3-319-12886-3_13, URL https://doi.org/10.1007/978-3-319-12886-3{_}13.

[14] Fernandez, P., Moura, R. C., Mengaldo, G., and Peraire, J., "Non-modal analysis of spectral element methods: Towards accurate and robust large-eddy simulations," *Computer Methods in Applied Mechanics and Engineering*, Vol. 346, 2019, pp. 43–62. doi:10.1016/J.CMA.2018.11.027, URL https://www.sciencedirect.com/science/article/pii/S0045782518305863.

[15] Cuong Nguyen, N., Terrana, S., and Peraire, J., "Large-Eddy Simulation of Transonic Buffet Using Matrix-Free Discontinuous Galerkin Method," *AIAA Journal*, 2022, pp. 1–18. doi:10.2514/1.j060459.

[16] Vila-Pérez, J., Van Heyningen, R. L., Nguyen, N.-C., and Peraire, J., "Exasim: Generating Discontinuous Galerkin Codes for Numerical Solutions of Partial Differential Equations on Graphics Processors," , 2022. doi:10.48550/ARXIV.2205.07824, URL https://arxiv.org/abs/2205.07824.

[17] Terrana, S., Nguyen, C., and Peraire, J., "GPU-accelerated Large Eddy Simulation of Hypersonic Flows," *AIAA Scitech 2020 Forum*, 2020, pp. AIAA–2020–1062. doi:10.2514/6.2020-1062, URL https://arc.aiaa.org/doi/abs/10.2514/6.2020-1062.

[18] Cook, A. W., and Cabot, W. H., "A high-wavenumber viscosity for high-resolution numerical methods," *Journal of Computational Physics*, Vol. 195, No. 2, 2004, pp. 594–601. doi:10.1016/j.jcp.2003.10.012, URL http://linkinghub.elsevier.com/retrieve/pii/S0021999103005746.

[19] Cook, A. W., and Cabot, W. H., "Hyperviscosity for shock-turbulence interactions," *Journal of Computational Physics*, Vol. 203, No. 2, 2005, pp. 379–385. doi:10.1016/j.jcp.2004.09.011, URL http://linkinghub.elsevier.com/retrieve/pii/S0021999104004000.

[20] Fiorina, B., and Lele, S. K., "An artificial nonlinear diffusivity method for supersonic reacting flows with shocks," *Journal of Computational Physics*, Vol. 222, No. 1, 2007, pp. 246–264. doi:10.1016/j.jcp.2006.07.020.

[21] Kawai, S., and Lele, S., "Localized artificial diffusivity scheme for discontinuity capturing on curvilinear meshes," *Journal of Computational Physics*, Vol. 227, No. 22, 2008, pp. 9498–9526. doi:10.1016/j.jcp.2008.06.034, URL http://linkinghub.elsevier.com/retrieve/pii/S0021999108003641.

[22] Kawai, S., Shankar, S. K., and Lele, S. K., "Assessment of localized artificial diffusivity scheme for large-eddy simulation of compressible turbulent flows," *Journal of Computational Physics*, Vol. 229, No. 5, 2010, pp. 1739–1762. doi:10.1016/j.jcp.2009.11.005, URL http://linkinghub.elsevier.com/retrieve/pii/S0021999109006160.

[23] Klöckner, A., Warburton, T., and Hesthaven, J. S., "Viscous shock capturing in a time-explicit discontinuous Galerkin method," *Mathematical Modelling of Natural Phenomena*, Vol. 6, No. 3, 2011, pp. 57–83. doi:10.1051/mmnp/20116303.

[24] Krivodonova, L., Xin, J., Remacle, J.-F., Chevaugeon, N., and Flaherty, J. E., "Shock detection and limiting with discontinuous Galerkin methods for hyperbolic conservation laws," *Appl. Numer. Math.*, Vol. 48, No. 3-4, 2004, pp. 323–338. doi:10.1016/j.apnum.2003.11.002, URL http://dx.doi.org/10.1016/j.apnum.2003.11.002.

[25] Mani, A., Larsson, J., and Moin, P., "Suitability of artificial bulk viscosity for large-eddy simulation of turbulent flows with shocks," *Journal of Computational Physics*, Vol. 228, No. 19, 2009, pp. 7368–7374. doi:10.1016/j.jcp.2009.06.040, URL http://linkinghub.elsevier.com/retrieve/pii/S0021999109003623.

[26] Olson, B. J., and Lele, S. K., "Directional artificial fluid properties for compressible large-eddy simulation," *Journal of Computational Physics*, Vol. 246, 2013, pp. 207–220. doi:10.1016/j.jcp.2013.03.026.

[27] Persson, P. O., and Peraire, J., "Sub-cell shock capturing for Discontinuous Galerkin methods," *44th AIAA Aerospace Sciences Meeting and Exhibit*, Reno, NV, 2006.

[28] Persson, P. O., "Shock Capturing for High-Order Discontinuous Galerkin Simulation of Transient Flow Problems," *21st AIAA Computational Fluid Dynamics Conference*, San Diego, CA, 2013.

[29] Fernandez, P., Nguyen, N. C., and Peraire, J., "A physics-based shock capturing method for unsteady laminar and turbulent flows," *56th AIAA Aerospace Sciences Meeting*, Orlando, Florida, 2018, pp. AIAA–2018–0062.

[30] Moro, D., Nguyen, N. C., and Peraire, J., "Dilation-based shock capturing for high-order methods," *International Journal for Numerical Methods in Fluids*, Vol. 82, No. 7, 2016, pp. 398–416. doi:10.1002/fld.4223.

[31] Nguyen, N. C., and Peraire, J., "An Adaptive Shock-Capturing HDG Method for Compressible Flows," *20th AIAA Computational Fluid Dynamics Conference*, American Institute of Aeronautics and Astronautics, Reston, Virigina, 2011, pp. AIAA 2011–3060. doi:10.2514/6.2011-3060, URL http://arc.aiaa.org/doi/abs/10.2514/6.2011-3060.

[32] Burbeau, A., Sagaut, P., and Bruneau, C. H., "A Problem-Independent Limiter for High-Order Runge-Kutta Discontinuous Galerkin Methods," *Journal of Computational Physics*, Vol. 169, No. 1, 2001, pp. 111–150. doi:10.1006/jcph.2001.6718.

[33] Cockburn, B., and Shu, C.-W., "TVB Runge-Kutta Local Projection Discontinuous Galerkin Finite Element Method for Conservation Laws II: General Framework," *Mathematics of Computation*, Vol. 52, No. 186, 1989, p. 411. doi:10.2307/2008474.

[34] Krivodonova, L., "Limiters for high-order discontinuous Galerkin methods," *Journal of Computational Physics*, Vol. 226, No. 1, 2007, pp. 879–896.

[35] Cockburn, B., and Shu, C. W., "The Runge-Kutta Discontinuous Galerkin Method for Conservation Laws V: Multidimensional Systems," *Journal of Computational Physics*, Vol. 141, No. 2, 1998, pp. 199–224. doi:10.1006/jcph.1998.5892.

[36] Lv, Y., and Ihme, M., "Entropy-bounded discontinuous Galerkin scheme for Euler equations," *Journal of Computational Physics*, Vol. 295, 2015, pp. 715–739. doi:10.1016/j.jcp.2015.04.026.

[37] Sonntag, M., and Munz, C. D., "Efficient Parallelization of a Shock Capturing for Discontinuous Galerkin Methods using Finite Volume Sub-cells," *Journal of Scientific Computing*, Vol. 70, No. 3, 2017, pp. 1262–1289. doi:10.1007/s10915-016-0287-5.

[38] Luo, H., Baum, J. D., and Löhner, R., "A Hermite WENO-based limiter for discontinuous Galerkin method on unstructured grids," *Journal of Computational Physics*, Vol. 225, No. 1, 2007, pp. 686–713. doi:10.1016/j.jcp.2006.12.017.

[39] Qiu, J., and Shu, C. W., "Runge-Kutta discontinuous Galerkin method using WENO limiters," *SIAM Journal on Scientific Computing*, Vol. 26, No. 3, 2005, pp. 907–929. doi:10.1137/S1064827503425298.

[40] Zhu, J., Qiu, J., Shu, C. W., and Dumbser, M., "Runge-Kutta discontinuous Galerkin method using WENO limiters II: Unstructured meshes," *Journal of Computational Physics*, Vol. 227, No. 9, 2008, pp. 4330–4353. doi:10.1016/j.jcp.2007.12.024.

[41] Zhu, J., Zhong, X., Shu, C. W., and Qiu, J., "Runge-Kutta discontinuous Galerkin method using a new type of WENO limiters on unstructured meshes," *Journal of Computational Physics*, Vol. 248, 2013, pp. 200–220. doi:10.1016/j.jcp.2013.04.012.

[42] Barter, G. E., and Darmofal, D. L., "Shock capturing with PDE-based artificial viscosity for DGFEM: Part I. Formulation," *Journal of Computational Physics*, Vol. 229, No. 5, 2010, pp. 1810–1827. doi:10.1016/j.jcp.2009.11.010, URL `http://linkinghub.elsevier.com/retrieve/pii/S0021999109006299`.

[43] Hartmann, R., "Higher-order and adaptive discontinuous Galerkin methods with shock-capturing applied to transonic turbulent delta wing flow," *International Journal for Numerical Methods in Fluids*, Vol. 72, 2013, pp. 883–894.

[44] Lv, Y., See, Y. C., and Ihme, M., "An entropy-residual shock detector for solving conservation laws using high-order discontinuous Galerkin methods," *Journal of Computational Physics*, Vol. 322, 2016, pp. 448–472. doi:10.1016/j.jcp.2016.06.052.

[45] Abbassi, H., Mashayek, F., and Jacobs, G. B., "Shock capturing with entropy-based artificial viscosity for staggered grid discontinuous spectral element method," *Computers & Fluids*, Vol. 98, 2014, pp. 152–163.

[46] Chaudhuri, A., Jacobs, G. B., Don, W. S., Abbassi, H., and Mashayek, F., "Explicit discontinuous spectral element method with entropy generation based artificial viscosity for shocked viscous flows," *Journal of Computational Physics*, Vol. 332, 2017, pp. 99–117. doi:10.1016/j.jcp.2016.11.042.

[47] Johnsen, E., Larsson, J., Bhagatwala, A. V., Cabot, W. H., Moin, P., Olson, B. J., Rawat, P. S., Shankar, S. K., Sjögreen, B., Yee, H., Zhong, X., and Lele, S. K., "Assessment of high-resolution methods for numerical simulations of compressible turbulence with shock waves," *Journal of Computational Physics*, Vol. 229, No. 4, 2010, pp. 1213–1237. doi:10.1016/j.jcp.2009.10.028, URL `http://linkinghub.elsevier.com/retrieve/pii/S0021999109005804`.

[48] Zahr, M. J., Shi, A., and Persson, P. O., "Implicit shock tracking using an optimization-based high-order discontinuous Galerkin method," *Journal of Computational Physics*, Vol. 410, No. 109385, 2020. doi:10.1016/j.jcp.2020.109385.

[49] Wheaton, B. M., Juliano, T. J., Berridge, D. C., Chou, A., Gilbert, P. L., Casper, K. M., Steen, L. E., Schneider, S. P., and Johnson, H. B., "Instability and transition measurements in the Mach-6 quiet tunnel," *39th AIAA Fluid Dynamics Conference*, 2009, pp. AIAA–2009–3559. doi:10.2514/6.2009-3559.

[50] Chynoweth, B. C., Schneider, S. P., Hader, C., Fasel, H., Batista, A., Kuehl, J., Juliano, T. J., and Wheaton, B. M., "History and progress of boundary-layer transition on a Mach-6 flared cone," *Journal of Spacecraft and Rockets*, Vol. 56, No. 2, 2019, pp. 333–346. doi:10.2514/1.A34285.

[51] Hader, C., and Fasel, H. F., "Direct numerical simulations of hypersonic boundary-layer transition for a flared cone: Fundamental breakdown," *Journal of Fluid Mechanics*, Vol. 869, 2019, pp. 341–384. doi:10.1017/jfm.2019.202.

[52] Ducros, F., Ferrand, V., Nicoud, F., Weber, C., Darracq, D., Gacherieu, C., and Poinsot, T., "Large-Eddy Simulation of the Shock/Turbulence Interaction," *Journal of Computational Physics*, Vol. 152, No. 2, 1999, pp. 517–549.

[53] Nguyen, N. C., and Peraire, J., "Hybridizable discontinuous Galerkin methods for partial differential equations in continuum mechanics," *Journal of Computational Physics*, Vol. 231, No. 18, 2012, pp. 5955–5988. doi:10.1016/j.jcp.2012.02.033, URL `http://linkinghub.elsevier.com/retrieve/pii/S0021999112001544`.

[54] Cockburn, B., and Shu, C.-W., "The local discontinuous Galerkin method for time-dependent convection-diffusion systems," *SIAM Journal on Numerical Analysis*, Vol. 35, No. 6, 1998, pp. 2440–2463. doi:10.1137/S0036142997316712, URL http://epubs.siam.org/doi/abs/10.1137/S0036142997316712.

[55] Bassi, F., Crivellini, A., Rebay, S., and Savini, M., "Discontinuous Galerkin solution of the Reynolds-averaged Navier-Stokes and k-ω turbulence model equations," *Computers & Fluids*, Vol. 34, No. 4, 2005, pp. 507–540.

[56] Bassi, F., and Rebay, S., "A high-order accurate discontinuous finite element method for the numerical solution of the compressible Navier-Stokes equations," *J. Comput. Phys.*, Vol. 131, No. 2, 1997, pp. 267–279. doi:10.1006/jcph.1996.5572, URL http://linkinghub.elsevier.com/retrieve/pii/S0021999196955722.

[57] Arnold, D. N., Brezzi, F., Cockburn, B., and Marini, L. D., "Unified analysis of Discontinuous Galerkin methods for elliptic problems," *SIAM Journal on Numerical Analysis*, Vol. 39, No. 5, 2002, pp. 1749–1779.

[58] Vila-Pérez, J., Giacomini, M., Sevilla, R., and Huerta, A., "Hybridisable Discontinuous Galerkin Formulation of Compressible Flows," *Archives of Computational Methods in Engineering*, Vol. 28, No. 2, 2021, pp. 753–784. doi:10.1007/s11831-020-09508-z, URL https://doi.org/10.1007/s11831-020-09508-z.

[59] Terrana, S., Nguyen, N. C., Bonet, J., and Peraire, J., "A hybridizable discontinuous Galerkin method for both thin and 3D nonlinear elastic structures," *Computer Methods in Applied Mechanics and Engineering*, Vol. 352, 2019, pp. 561–585. doi:10.1016/j.cma.2019.04.029, URL https://www.sciencedirect.com/science/article/pii/S0045782519302324.

[60] Alexander, R., "Diagonally implicit Runge-Kutta methods for stiff ODEs," *SIAM J. Numer. Anal.*, Vol. 14, 1977, pp. 1006–1021.

[61] Knoll, D. A., and Keyes, D. E., "Jacobian-free Newton-Krylov methods: A survey of approaches and applications," , 2004. doi:10.1016/j.jcp.2003.08.010.

[62] Grepl, M. a., Maday, Y., Nguyen, N. C., Patera, A. T., and C., N. N., "Efficient reduced-basis treatment of nonaffine and nonlinear partial differential equations," *ESAIM: Mathematical Modelling and Numerical Analysis*, Vol. 41, No. 3, 2007, pp. 575–605. doi:10.1051/m2an:2007031, URL http://www.esaim-m2an.org/10.1051/m2an:2007031http://journals.cambridge.org/abstract{_}S0764583X07000313.

[63] Rozza, G., Huynh, D. B. P., and Patera, A. T., "Reduced basis approximation and a posteriori error estimation for affinely parametrized elliptic coercive partial differential equations: Application to transport and continuum mechanics," *Archives Computational Methods in Engineering*, Vol. 15, No. 4, 2008, pp. 229–275.

[64] Nguyen, N. C., "A multiscale reduced-basis method for parametrized elliptic partial differential equations with multiple scales," *Journal of Computational Physics*, Vol. 227, No. 23, 2008, pp. 9807–9822. doi:10.1016/j.jcp.2008.07.025, URL http://linkinghub.elsevier.com/retrieve/pii/S0021999108004087http://www.scopus.com/inward/record.url?eid=2-s2.0-53349103005{&}partnerID=40{&}md5=64852a2fac4b34c956379f980e2cf264.

[65] Kraichnan, R. H., "Diffusion by a random velocity field," *Physics of Fluids*, Vol. 13, No. 1, 1970, pp. 22–31. doi:10.1063/1.1692799.

[66] Béchara, W., Bailly, C., Lafon, P., and Candel, S. M., "Stochastic approach to noise modeling for free turbulent flows," *AIAA Journal*, Vol. 32, No. 3, 1994, pp. 455–463. doi:10.2514/3.12008.

[67] Bailly, C., and Juvé, D., "A stochastic approach to compute subsonic noise using linearized euler's equations," *5th AIAA/CEAS Aeroacoustics Conference and Exhibit*, 1999, pp. 496–506. doi:10.2514/6.1999-1872.

[68] Zhang, C. H., Tang, Q., and Lee, C. B., "Hypersonic boundary-layer transition on a flared cone," *Acta Mechanica Sinica/Lixue Xuebao*, Vol. 29, No. 1, 2013, pp. 48–54. doi:10.1007/s10409-013-0009-2.